Fractal Statistics of Cloud Fields

ROBERT F. CAHALAN

Laboratory for Atmospheres, Goddard Space Flight Center, Greenbelt, Maryland

JOACHIM H. JOSEPH

Laboratory for Atmospheres, Goddard Space Flight Center, Greenbelt, Maryland; and Department of Geophysics and Planetary Sciences, Beverly and Raymund Sackler Faculty of Exact Sciences, Tel-Aviv University, Ramat-Aviv, Israel

(Manuscript received 5 November 1987, in final form 14 June 1988)

ABSTRACT

Landsat Multispectral Scanner (MSS) and Thematic Mapper (TM) data, with 80 and 30 m spatial resolution, respectively, have been employed to study the spatial structure of boundary-layer and intertropical convergence zone (ITCZ) clouds. The probability distributions of cloud areas and cloud perimeters are found to approximately follow a power-law, with a different power (i.e., fractal dimension) for each cloud type. They are better approximated by a double power-law behavior, indicating a change in the fractal dimension at a characteristic size which depends upon cloud type. The fractal dimension also changes with threshold. The more intense cloud areas are found to have a higher perimeter fractal dimension, perhaps indicative of the increased turbulence at cloud top. A detailed picture of the inhomogeneous spatial structure of various cloud types will contribute to a better understanding of basic cloud processes, and also has implications for the remote sensing of clouds, for their effects on remote sensing of other parameters, and for the parameterization of clouds in general circulation models, all of which rely upon plane-parallel radiative transfer algorithms.

1. Introduction

This paper focuses on cloud spatial structure—how it varies with a change in scale or resolution for various cloud types. A number of theoretical studies have shown the sensitivity of cloud radiative properties to their spatial structure. (See for example, Aida 1977; Davies 1978; McKee and Klehr 1978; Reynolds et al. 1978; Harshvardan and Weinman 1982; Joseph 1985). To produce a tractable problem, such studies typically restrict themselves to a lattice of bar clouds or cubic clouds, having a small number of adjustable length scales. By contrast, actual cloud fields are typically observed to be extremely irregular and/or fragmented at all scales.

A useful notion for discussing such cloud structure is that of a "scaling fractal" (Mandelbrot 1983 and references therein), which is a set or object which is extremely irregular on all scales, while at the same time statistically invariant under certain transformations of scale. The simplest examples are the statistically "self-similar" fractals (Mandelbrot 1983, p. 350)—geometrical patterns (other than Euclidean lines, planes and surfaces) with no intrinsic scale, so that no matter how closely you inspect them, they always look the same, at least in a statistical sense. If one measures the perimeter of a self-similar fractal at successively higher resolution, with a ruler of decreasing length ϵ, the result increases as ϵ^{1-D}, where the scaling exponent D may be interpreted as a "fractal dimension". (For a discussion of various types of dimensions in the context of chaotic attractors see Farmer et al. 1983.) While self-similar fractals are statistically isotropic, the so-called "self-affine" fractals scale differently in different directions (e.g., see Mandelbrot 1986). The most general scaling fractals are the multidimensional fractals, or "multifractals" (Hentschel and Procaccia 1983 and Frisch and Parisi 1985) which exhibit a spectrum of fractal dimensions.

Lovejoy (1982) has presented empirical evidence that clouds are statistically self-similar in the horizontal plane from 1000 km down to 1 km, with a fractal dimension of approximately $4/3$. If this were strictly true, than a satellite image of a cloud field, taken over a uniform dark ocean background with no evident geographical features, would be statistically indistinguishable from an image of any small portion of the scene if it had the same number of pixels as the original. Schertzer and Lovejoy (1986) have argued that clouds are self-affine in a vertical plane, and have considered multifractal cloud models (Schertzer and Lovejoy 1988 and references therein). These idealizations provide important alternatives to the simple plane-parallel or lattice cloud fields, and it is important to consider their consequences and limitations.

Clearly horizontal self-similarity must break down as we go to smaller scales, since the microscopic cloud structure of cloud droplets differs from the macroscopic structure of individual clouds observed by eye or by

Corresponding author address: Dr. Robert F. Cahalan, Code 613, NASA/Goddard Space Flight Center, Greenbelt, MD 20771

satellite. At what scales and in what manner does this breakdown occur, and what physical processes control the scales? Rhys and Waldvogel (1986) confirmed Lovejoy's result for midlatitude storm systems, but also found a sharp transition to more smooth behavior below a characteristic scale of about 1 km. Are there also characteristic scales for subtropical and tropical cloud types?

A second important question concerns the universality of the fractal dimension. Various climatological regimes exhibit cloud types having distinct spatial and temporal characteristics. For example, in the North Pacific Ocean one finds a band of storm track cloudiness extending from the coast of Japan, a region of stratocumulus off the California coast, fair weather cumulus in the subtropics, and a band of deep convective clouds centered at 5°N. (See, for example, Cahalan et al. 1981, and Hahn et al. 1982.) It would seem natural to expect such distinct structures to exhibit distinct fractal characteristics. Do different cloud types have different fractal dimensions? Rhys and Waldvogel (1986) conjecture that all cloud types have the same fractal dimension above the characteristic length. This is not the case for subtropical boundary layer clouds, as we shall see. These clouds undergo abrupt changes in scaling behavior at certain characteristic scales, but exhibit distinctly different fractal dimensions over the full range of scales accessable to Landsat.

Finally, clouds are three-dimensional objects, and cloud structure often varies considerably from cloud base to cloud top. In the case of fair weather cumulus this vertical variation is evident to the eye. They are flat at the base where parcels reach the lifting condensation level, but have considerable small-scale variations at cloud top. Vertical variations in structure are less obvious for nocturnal stratocumulus, but show up for example in the temperature variance, which has a sharp peak at cloud top, where the radiative loss drives the turbulence (Caughey et al. 1982). How are such vertical variations in cloud structure reflected in fractal dimensions or other scaling parameters?

To make some progress on these questions we have studied the spatial structure of marine boundary-layer and intertropical convergence zone (ITCZ) clouds with the help of the high spatial resolution of Landsat Multispectral scanner (MSS) and Thematic Mapper (TM) instruments. We emphasize that all of our conclusions about cloud structure are based upon our analysis of the spatial distribution of cloud *radiative properties* as observed by Landsat. The distribution of cloud *liquid water* is of course more fundamental, since the radiative properties are computable from the distribution of liquid water, traditionally by specifying microscopic properties like drop sizes, and macroscopic properties like the distribution of optical depth, cloud height, etc.. Determining these properties from the radiation by inversion is extremely difficult in the non–plane-parallel case, and no simple one-to-one correspondence between brightness and liquid water is likely. In particular, there may be small-scale variations of liquid water to which the Landsat data are completely insensitive. Analysis of data on cloud liquid water during the FIRE field program should help decipher some aspects of the important relationship between cloud radiation and liquid water. In line with common usage, we shall use the word "cloud" to refer to the satellite-observed radiative effects of the liquid water, rather than the liquid water itself.

In section 2 we describe the Landsat data and summarize our analysis techniques. Section 3 describes our results for the area distributions and perimeter fractal dimensions, including dependence on cloud type and vertical level. As we shall see, the area distributions increase rapidly down to the smallest detectable size. [See also, for example, Plank (1969), and Hozumi et al. (1982).] The probability distributions of cloud areas and cloud perimeters are approximated by a double power-law, indicating a change in the fractal dimension at a characteristic size. This size as well as the fractal dimensions vary with cloud type. The fractal dimension also changes with the reflectivity threshold. As the threshold is raised from cloud base to cloud top, the perimeter fractal dimension increases, perhaps indicative of the increased turbulence at cloud top. Finally, in section 4 we summarize our results and conclusions.

2. Data and analysis technique

The major source of data for this investigation is the Landsat thematic mapper (TM) and multispectral scanner (MSS) instruments. The results given here are primarily from the TM, but have been checked by independent analysis of data from the MSS. The MSS lacks a thermal band and has somewhat less spatial and radiometric resolution, but has a database beginning in 1972, 10 yr before TM. The nearest-neighbor spacing distribution from MSS is reported in Joseph and Cahalan (1988), and similar TM results have been given in Cahalan (1988). The present paper focuses specifically on the scaling properties derived from the perimeter and area distributions. The TM analysis was carried out at the Goddard Laboratory for Atmospheres using techniques which are described in detail in subsection a. The MSS analysis was carried out at Tel Aviv University, and is described in detail elsewhere (Joseph and Cahalan 1988), but summarized briefly in subsection b. The TM analysis is emphasized in this paper, but it is shown in subsection 3b that the MSS results are not significantly different than the TM ones, despite the different technique employed.

a. TM analysis at Goddard Laboratory for Atmospheres

Landsat TM data has a resolution of 0.12 km in the thermal emitted band (10.4 to 12.5 microns) and 0.03

in the visible and near IR reflected bands (0.45 mm to 0.52 mm, 0.52 mm to 0.59 mm, 0.63 mm to 0.67 mm, 0.76 mm to 0.90 mm, 1.55 mm to 1.75 mm, and 2.08 mm to 2.35 mm). The field of view is 185 km, somewhat smaller than a GCM gridbox, with about 6100 pixels on a side for the reflected bands, and 1600 for the thermal band.

The TM radiances are digitized into 256 intensity levels, with one byte per pixel per band. Thus each reflected band of 6100 pixels on a side represents about $(6100)^2$ bytes or about 36 megabytes, while the thermal band represents about $(1600)^2$ bytes or about 2.5 megabytes, for a total of 218.5 megabytes per scene. Each scene is split into four quarters, and each quarter requires one 6250 bpi tape.

The available TM data consisted of 19 Landsat-5 scenes, with locations shown at the solid dots in Figure 1. (Eleven Landsat-4 TM scenes east of Florida were also analysed at Tel-Aviv.) Eleven TM scenes were acquired along a contiguous strip from 25°N to 27°S over the eastern Pacific Ocean. This strip spans persistent climatological regimes of stratocumulus cloud fields, fair weather cumulus, ITCZ, and storm track cloudiness. Additional acquisitions include two California stratocumulus scenes and six fair weather cumulus scenes (three along the Atlantic coast, one in the Gulf of Mexico, one over Lake Michigan, and one over Amazonia). New scenes are also being acquired in coordination with the observational programs associated with the First ISCCP Regional Experiment (FIRE).

Processing of the data proceeded in several steps:

1) determine a cloud reflectivity threshold (see below) and identify each pixel as "cloudy" or "not cloudy", thus producing a binary image;

2) identify contiguous clear and cloudy areas in the binary image, determine various characteristics of each area, and store results in an ancillary file with one record per area;

3) determine statistical distributions from each ancillary file and fit the distributions to determine cloud parameters;

4) compute statistics of cloud parameters for various cloud types, thresholds, etc.

Two thresholds are determined for each scene—one appropriate for cloud "base" and one for cloud "top". If the cloud fraction is known independently, then the cloud base threshold can be adjusted to produce the correct cloud fraction. The cloud fraction of single-layer clouds such as stratocumulus and fair weather cumulus can be determined from the thermal band by the spatial coherence method (Coakley and Bretherton 1982).

Figure 2 illustrates this method of determination of the cloud base threshold for a scene from the FIRE marine stratocumulus experiment on July 7 1987. Figure 2a shows a histogram of the thermal infrared brightness temperature of a region 512 pixels (61.44 km) on a side, with a cloud top peak at about 11°C and a "surface" peak at about 16°C. Grouping the pixels into 4×4 pixel arrays and computing the mean and standard deviation for each of the 128^2 arrays gives us the scatter plot shown in figure 2b, which forms an "arch" between the cloud covered pixel arrays in the "cold foot" of the arch and the clear pixel arrays in the "hot foot". Even at Landsat resolution, most of the pixels fall in the region between the feet associated with partially cloudy pixels. From the distribution of points in each foot of the arch, one determines four parameters: the cloud top radiance and its error, $I_c \pm \Delta I_c$,

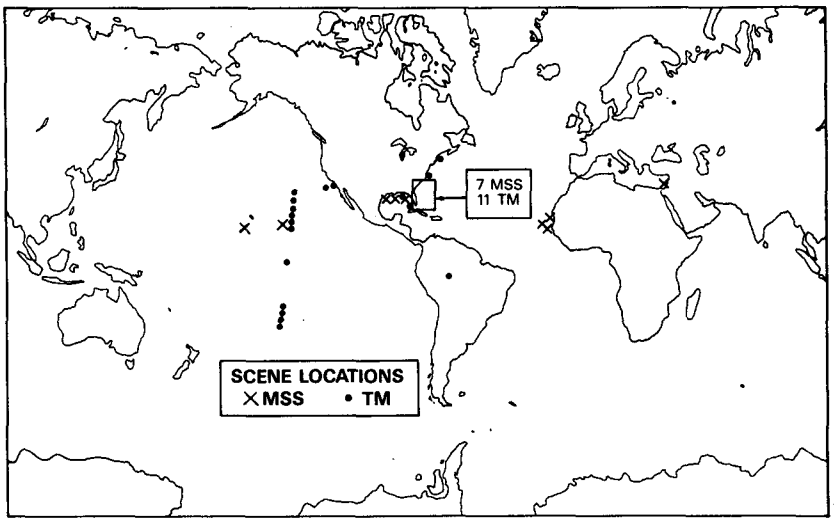

FIG. 1. Locations of scenes from the Landsat-3 MSS, Landsat-4 TM and Landsat-5 TM instruments used in the analysis described in the text.

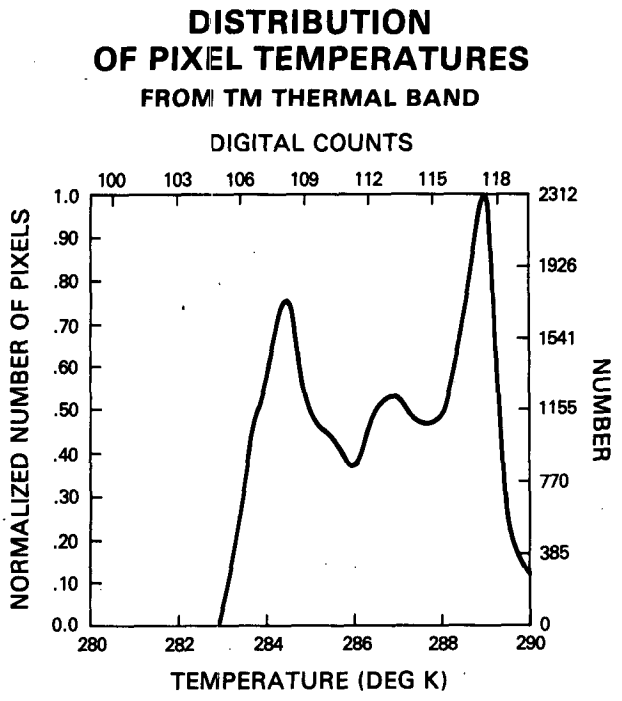

FIG. 2(a). Histogram of thermal infrared brightness temperatures from TM band 6 for a region 512 pixels (61.44 km) on a side at the edge of a stratocumulus cloud scene during the FIRE marine stratocumulus experiment on 7 July 1987. The histogram shows a cloud top peak at about 10°C and a "surface" peak at about 15°C.

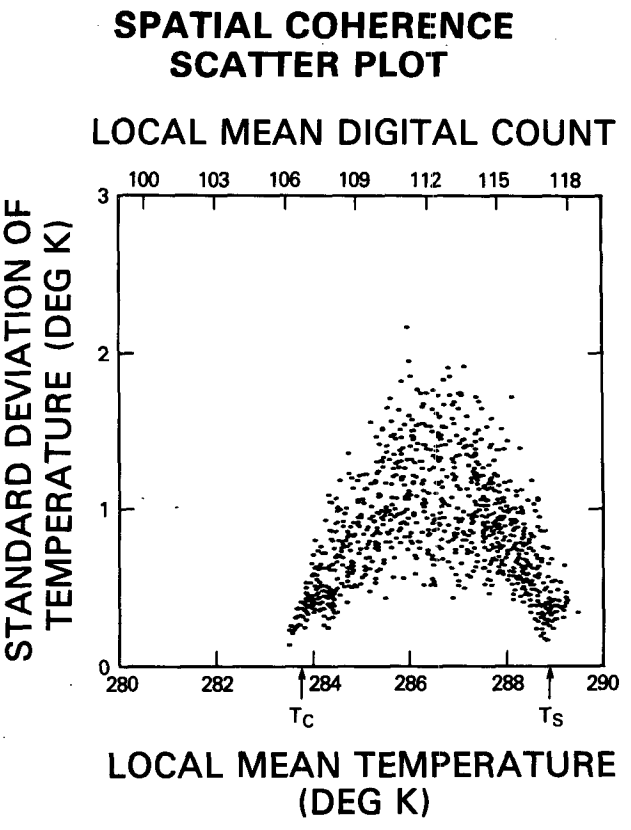

FIG. 2(b). The usual spatial coherence plot, which is a scatter plot of mean versus standard deviation of 4 by 4 pixel arrays from the same 512 by 512 scene used in Fig. 2(a). One sees the usual "arch" connecting the low variance "cold foot", corresponding to completely cloud covered pixel arrays, with the low variance "hot foot", corresponding to completely cloud free pixel arrays. Even at Landsat resolution most pixels fall in the region between the feet, corresponding to partially cloudy pixel arrays. The cloud fraction may be computed from the mean radiance in each of the feet and the overall mean, as given in Eq. 2.1 of the text, and the error is determined by the width of the feet, as given in Eq. 2.2.

and the surface radiance and its error $I_s \pm \Delta I_s$. The cloud fraction, A_c, is then given by

$$A_c = (I_s - \bar{I})/(I_s - I_c), \tag{2.1}$$

where $\bar{I}$ is the average thermal infrared radiance over the scene. If we neglect the error in $\bar{I}$, the error in A_c is given by

$$\Delta A_c = \pm\{(A_c \Delta I_c)^2 + [(1 - A_c)\Delta I_s]^2\}^{1/2}/(I_S - I_c). \tag{2.2}$$

The arch parameters determined from Fig. 2b give A_c = 45% and ΔA_c = 2%. (Note that since only radiance differences appear, the bias due to the atmosphere may be neglected.) The TM database gave values of A_c ranging from 6% to 80%, with a mean of 31.3%, and values of ΔA_c ranging from 2% to 6%, with a mean of 3.36%.

To determine the cloud base threshold associated with this value of A_c, we first compute the cumulative distribution—the fraction of pixels having thermal radiances below a given value—by integrating figure 2a to obtain figure 2c. The two values on the vertical axis at $A_c \pm \Delta A_c$ = 45% ± 2% determine cloud base thresholds on the horizontal axis at 12.9°C ± 0.16°C. In the reflected channels the cloud fraction corresponds to reflectances above a given value, so we assign $1 - (A_c \pm \Delta A_c)$ to the cumulative distribution to determine the cloud base brightness threshold, as shown for band 7 in Fig. 2d.

The cloud base temperature estimated by the above method is within about 1°C of aircraft measurements taken during the FIRE stratocumulus experiment (P. Austin, personal communication), and is probably a good approximation for most boundary-layer clouds. However, the presence of cirrus anvils, common in deep convection, can make the cloud fraction seen in the infrared differ considerably from that seen in the visible, and thus produce errors in the estimated cloud base temperature. Thus, our results for ITCZ clouds are subject to larger errors that those for stratocumulus and fair weather cumulus.

Once the cloud base brightness threshold is determined, the cloud top brightness threshold is found by raising the brightness threshold until the fraction above the top threshold becomes a given ratio of the fraction above the base threshold. The ratio has been set at

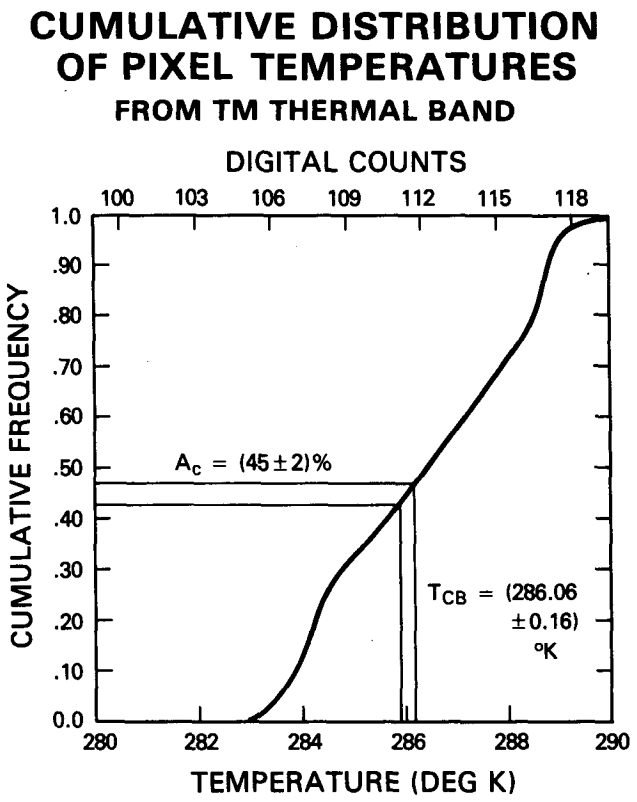

FIG. 2(c). The cumulative distribution of thermal infrared brightness temperatures determined by integrating Fig. 2(a). This gives the fraction of pixels colder than each given temperature. On the vertical axis we select the cloud fraction (45% ± 2%), and the cumulative distribution determines the associated cloud base temperature on the horizontal axis (12.9°C ± 0.16°C).

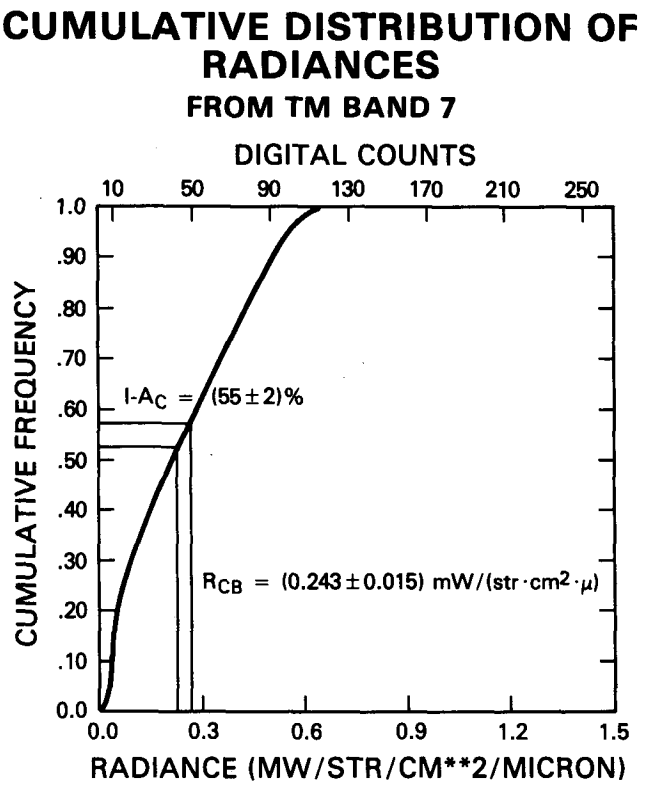

FIG. 2(d). The cumulative distribution of reflected radiances from TM band 7 for the same scene used in Fig. 2(c). This gives the fraction of pixels darker than each given radiance. On the vertical axis we select the cloud-free fraction determined from Fig. 2(b) (55% ± 2%), and the cumulative distribution determines the associated cloud-base radiance on the horizontal axis (0.243 ± 0.015 mW cm^{-2} sr^{-1} μ^{-1}).

10%, which separates the thresholds sufficiently to give a good estimate of the sensitivity of our results to changes in threshold.

When the cloud fraction cannot be determined independently, due to lack of thermal data or the presence of multilevel clouds, as in the ITCZ, then the cloud base threshold is chosen just above the surface peak in the brightness histogram (see also subsection (b). Since we have emphasized the sensitivity of cloud spatial structure to changes in threshold—by presenting our results for two widely separated thresholds—the precise values of these thresholds are not of primary importance in this paper. We should emphasize again, however, that the cloud base temperatures for the ITCZ clouds are expected to have large errors, which contribute to the large spread in the ITCZ results discussed in section 3.

Eventually a file of contiguous areas is produced from each chosen TM subscene. Each record of this area file contains an area identification number, area type (cloud/no-cloud), area size in pixels and square kilometers, number of perimeter pixels of various types, center-of-mass coordinates, and an edge flag indicating whether the cloud boundary intersects the scene boundary. Each such file contains thousands of records, and typically there are two or three files for each threshold and each band of a full TM scene. A total of 175 189 clouds from Landsat-5 TM were analyzed.

b. MSS analysis at Tel-Aviv University

The MSS has four bands—the blue band MSS 4 (0.5–0.6 mm), the red band MSS 5 (0.6–0.7 mm), a near IR band MSS 6 (0.7–0.8 mm) and a second near IR band MSS 7 (0.8–1.1 mm). Each MSS scene has a field of view of 185 by 170 km, with the short axis oriented parallel to the satellite track. The sun-synchronous near-polar orbit of the satellite is at an altitude of about 920 km, with a nominal 0930 LST equator crossing time. The orbit repeat cycle is 18 days. Each spectral band consists of six-bit digitized brightness values for about 10 million 57 m pixels. Since the gain is optimized for land surface observations, clouds typically saturate the instrument. The maximum measurable radiance corresponds to a Lambertian white reflector with an efficiency of 50% for a solar zenith angle of 45 degrees.

The available MSS data consisted of 37 Landsat-3 scenes; ten are over land and will be analyzed in the future. Three images over ocean have been returned for reprocessing or exchange due to severe errors in the data. Eight cannot be analyzed with sufficient precision due either to insufficient cloudiness (less than 0.5%) or too inhomogeneous ocean or island backgrounds. Thus, 16 MSS scenes from Landsat-3 have been fully analyzed for this study. The locations are shown in Fig. 1—nine indicated by crosses in the Pacific, Gulf of Mexico, Atlantic and Mediterranean, and seven clustered together in a region off the coast of Florida.

First, black and white prints of selected bands are used for quality checks, navigation, and detailed site selection prior to analysis of the digital data. Since the MSS has no thermal band, cloud fraction cannot be computed by spatial coherence analysis, as is done with the TM data. Instead, bands 4 and 7 (and sometimes 6) are analyzed separately to check the results of one band versus the others with respect to total number of clouds, total cloud area, and the fraction of clouds smaller than four pixels in area, taken as a measure of "noise" in the data. As the threshold is lowered, the noise increases slowly up to a point, beyond which it begins to increase dramatically. The threshold is set just above this point, and also tuned so that the cloud fraction and number of clouds agree from band to band. [For details, see Joseph and Cahalan (1988); also Wielicki and Welch (1986).]

Once the threshold is determined for each band of an image, we identify each pixel as "cloudy" or "not cloudy" and a binary image is produced. Then contiguous clear and cloudy areas are identified in the binary image by a running scan of three lines down the image. The characteristics of each area are recorded and stored in an ancillary file. Each record of this area file contains an area identification number, area type (cloud/no-cloud or hole-in-cloud), area size in pixels, area of pixel, number of perimeter pixels, coordinates of the center of brightness, coordinates of the window in which the cloud is inscribed, and finally an edge flag indicating whether the cloud boundary intersects the scene boundary. Each such file contains thousands of records for each band analyzed. Histograms are computed from the ancillary files, and the results fitted to assumed distributions to determine the cloud field parameters.

Landsat-4 TM data were processed along similar lines. A total of 127 555 clouds from Landsat-3 MSS and 102 854 from Landsat-4 TM were analyzed. The statistical results presented in the following two sections are computed from these databases of over 100 000 cloud areas for each of Landsat-3 MSS, Landsat-4 TM and Landsat-5 TM.

3. Area and perimeter fractal dimensions

It is important to emphasize that the various cloud properties discussed here were determined (and their threshold dependence studied) for each Landsat scene *separately,* so that it was possible to isolate the various cloud types. The coarse resolution typical of meteorological satellites requires a large field of view if one is to include more than a small number of cloud areas, but then one is forced to include a number of cloud types in a given scene. By contrast, the high-resolution Landsat image allows one to avoid this problem of "mixing", while still resolving thousands of cloud areas in the 180 km scene. In determining each parameter, we neither pooled data from different scenes, nor did we employ variable thresholds in a single scene, either of which might have caused the inadvertent "mixing" of fractals of differing dimensions.

We first discuss the TM results, which have been computed for three cloud types—fair weather cumulus, stratocumulus, and ITCZ (deep cumulus) clouds—and for both cloud base and cloud top thresholds. We then give the MSS results for fair weather cumulus cloud bases, and compare to the TM.

a. TM results for various cloud types

We first examine the distribution of cloud base areas. Since the larger areas are far less common, it is convenient to use area bins of increasing width. We do this by changing variables from area to the logarithm of the square root of the area, and then using bins of equal width. If the area is denoted as a, let

$$x = \log(\sqrt{a}). \tag{3.1}$$

Then the distribution of a is related to the distribution of x as

$$n(a) = n(x)dx/da = n(x)/(2a). \tag{3.2}$$

How do we expect $n(x)$ to behave in the case of scaling fractals? It can be shown that the distributions in that case must be power law (see, for example, Falconer 1985). Mandelbrot (1983, p.117f) has shown that for a simple class of recursively generated scaling fractals one obtains a more specific relation, termed the "Korcak law", given by

$$\int_a^\infty n(a')da' = Fa^{-B}, \tag{3.3}$$

where the exponent B is given by

$$B = d/2 \tag{3.4}$$

where d represents the fractal dimension of the cumulative perimeter of all the individual areas, and is related to the fractal dimension of individual perimeters, d_p, by

$$1 \leqslant d_p < d \leqslant 2. \tag{3.5}$$

Taking the derivative of (3.3) with respect to a to obtain $n(a)$, multiplying by $2a$ to obtain $n(x)$, and taking the log of the resulting expression leads to

$$\log(n(x)) = -2Bx + \text{constant}. \tag{3.6}$$

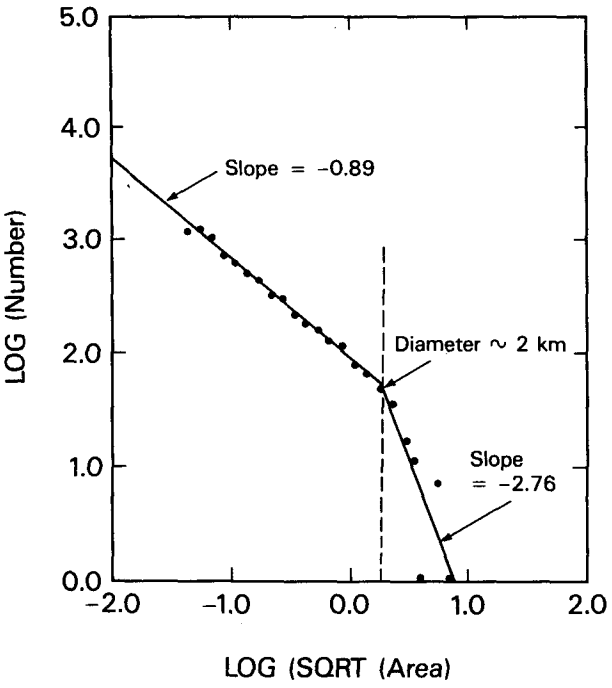

FIG. 3. Histogram of contiguous cloud base areas, defined by a reflectance threshold, for a fair weather cumulus cloud field off the coast of South Carolina. The logarithm of the number vs the logarithm of the square root of the area is plotted, and fit to two straight lines, with slopes and the location of the break determined by least squares.

The power-law relations (3.1) and (3.6) follow from the assumption of scale invariance alone, while the interpretation of the exponent B as a fractal dimension in (3.4) and (3.5) is not generally valid. Lovejoy and Mandelbrot (1985) have discussed a "fractal sum of pulses" (FSP) model in which $B = 0.5$, and $d_p = 1.4 > 2B$, contradicting (3.5). Lovejoy and Schertzer (1985) have described a more general "scaling cluster of pulses" (SCP) model giving $B = 0.75$, and $d_p = 1.5 = 2B$. The SCP model agrees with the GATE rainfall data for B, but produces somewhat too large a value of d_p (1.5 compared with the GATE value 1.35).

How do these results compare to the TM cloud data? Figure 3 shows an example of a plot of $\log(n)$ versus x for cloud base areas in a scene off the coast of South Carolina containing more than 10 000 fair weather cumulus clouds. (Results in Figs. 3–6 are from TM band 7 of Landsat-5.) Also shown is a double straight line fit, with the slopes and location of the break determined by minimizing the mean square error. The great majority of clouds, those smaller than 2 km in diameter, closely follow a straight line with slope −0.89 (i.e., $B = 0.445$) with very small error. The population of clouds larger than 2 km in diameter falls off more rapidly, and can be fit with a straight line of slope −2.76, though with more error in the fit. The change in slope represents a clear violation of scale invariance.

Similar behavior to that shown in Fig. 3 has been observed in a wide variety of fair weather cumulus cloud scenes. The typical break diameter is somewhat smaller than that shown, with the average being about 0.5 km (see also Joseph and Cahalan 1988). Scale invariance appears to be an excellent assumption for the smaller clouds down to the limit of our resolution. However, since the slope in this region is flatter than −1, so that $B < 0.5$, this would give $d < 1$, so that the simple class of scaling fractals mentioned above cannot apply. The FSP and SCP models must also be excluded, since they both give $B \geqslant 0.5$.

Figure 4a summarizes our results for the power, $2B$, of the cloud base area distributions. The value of $2B$ is determined by fitting two straight lines by least squares as in Fig. 3. The breakpoint is again determined by minimizing the mean square error. In Figure 4a we show the average value of $2B$ for all available scenes of a given cloud type, for three cloud types, namely stratocumulus (StCu), fair weather cumulus (FWCu), and deep cumulus (ITCZ). For each cloud type, an average slope is shown for clouds below the break point (StCu<, for example) as well as those above (StCu>). The position of the break varies from scene to scene, but is typically at about 0.5 km for FWCu , and 1 to 2 km for StCu and ITCZ. (Recall that, as discussed above, the ITCZ cloud bases are poorly determined due to the presence of cirrus anvils.) In addition to the average slope in each category, the standard deviation of the slopes was also computed, and vertical lines

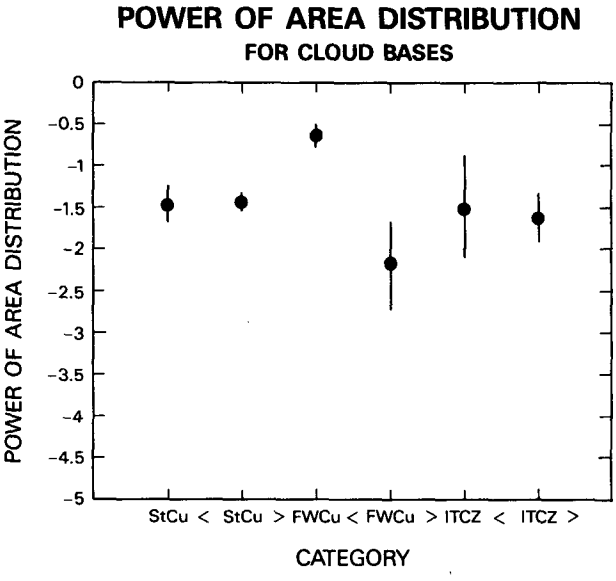

FIG. 4(a). Summary of cloud base area distributions. The slopes (referred to as $2B$ in the text), were determined as in Fig. 3 and averaged over all available scenes of a given cloud type, for the three cloud types described in the text. A value of the slope is obtained for smaller (<) and larger (>) areas for each cloud type. The vertical lines extend one standard deviation above and below the mean. Note that small and large clouds have significantly different slopes for both fair weather cumulus and ITCZ. Only stratocumulus are consistent with scale invariance.

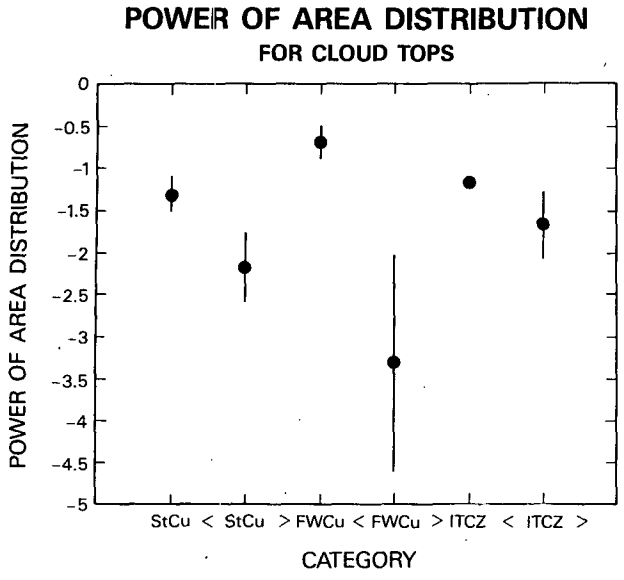

FIG. 4(b). As in Fig. 4(a), but for cloud top areas. Comparing with Fig. 4(a), we see that the means differ by less than a standard deviation, so that there is no significant dependence on threshold, with the exception of the larger stratocumulus areas, which drop off more rapidly for the higher threshold.

plotted one standard deviation above and below the mean. (Each slope in the average was weighted by the number of clouds in the fit, but this weighting makes no qualitative difference in the results.)

If slopes within one standard deviation of each other are considered to be indistinguishable, we can see from Fig. 4a that both stratocumulus and ITCZ clouds are consistent with

$$n \sim (\sqrt{a})^{-1.5}. \tag{3.7}$$

However, this conclusion is somewhat premature for the ITCZ since the cloud base is poorly determined and the errors are quite large. The fair weather cumulus behave as

$$n \sim \begin{cases} (\sqrt{a})^{-0.6}, & (\sqrt{a}) < 0.5 \text{ km} \\ (\sqrt{a})^{-2.3}, & (\sqrt{a}) > 0.5 \text{ km}. \end{cases} \tag{3.8}$$

Figure 4b shows a similar plot as in 3a, but for cloud tops rather than cloud bases. The only significant change in raising the threshold from cloud base to cloud top is that StCu and ITCZ cloud tops are now also inconsistent with the scaling fractal assumption, but behave like FWCu, with a more rapid decrease for larger sizes. Unlike FWCu, however, the slopes still lie between 1 and 2, and so may allow some kind of dimensional interpretation, or an FSP or SCP fractal model.

The fractal dimension of the individual perimeters, d_p, may be obtained by considering the perimeter length, p, as a function of the area a, or equivalently of x. For smooth shapes (circles, squares, etc.), $d_p = 1$ and the perimeter is proportional to $\sqrt{a}$. For a self-similar scaling fractal the perimeter is proportional to $(\sqrt{a})^{d_p}$. Thus

$$\log(p) = d_p x + \text{const.} \tag{3.9}$$

Figure 5 shows a scatter plot of $\log(p)$ versus x for the same FWCu cloud scene used in Fig. 3. Using the same cutoff area found in Fig. 3 (2 km), the points are fit to two straight lines by least squares. Three different algorithms were used to estimate cloud perimeters: 1) counting the total number of perimeter pixels and multiplying by the perimeter diameter; 2) summing the lengths of all perimeter edges adjacent to "non-cloud" pixels; and 3) summing perimeter edges after replacing corners by diagonals. These approximations give identical results for clouds larger than about 12 pixels, or 100 m on a side. Clouds smaller than 12 pixels in area were excluded from the analysis, since they produced a slope sensitive to the perimeter algorithm, while the slopes shown here are insensitive to the perimeter algorithm. The slope for those clouds between 100 m and 2 km is close to $4/3$, while that for the larger clouds is about 1.6. Thus for the smaller clouds $d_p > d$, which again is inconsistent with the result given above for a simple class of scaling fractals.

Figure 6a summarizes the results for the fractal dimension of cloud perimeters, d_p, and has a similar for-

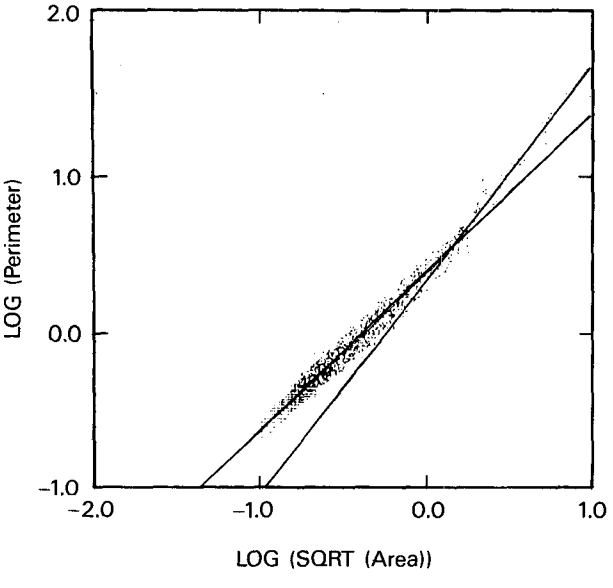

FIG. 5. Log–log plot of cloud base perimeter as a function of the square root of the area for the same scene as in Fig. 1. The points are fit to two straight lines by least squares, using the same cutoff area found in Fig. 3. The slope, or so-called "fractal dimension" of the perimeter, was found to depend on how the perimeter is defined for clouds smaller than about 12 pixels in area, and these were therefore excluded from the analysis.

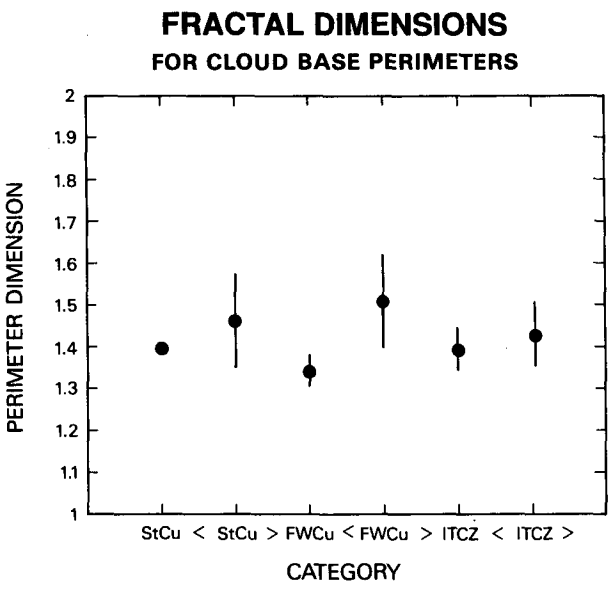

FIG. 6(a). Summary of cloud base perimeter fractal dimensions. The slopes, determined as in Fig. 5 and averaged over all available scenes of a given cloud type, are shown for the three cloud types described in the text. A value of the slope is obtained for smaller (<) and larger (>) areas for each cloud type. The vertical lines extend one standard deviation above and below the mean. Note that the smaller fair weather cumulus clouds have a perimeter fractal dimension of $d_p \approx 4/3$, while $d_p > 1.5$ for the larger ones. The cloud base perimeters of the other two cloud types are consistent with scaling, with a dimension of $d_p \approx 1.4$.

mat to Figure 4a. As in 4a, we see that both StCu and ITCZ are consistent with a single dimension,

$$d_p \sim 1.4\text{–}1.5, \tag{3.10}$$

while for FWCu we have

$$d_p \sim \begin{cases} 1.33, & x < 0.5 \text{ km} \\ 1.55, & x > 0.5 \text{ km}. \end{cases} \tag{3.11}$$

The perimeter fractal dimensions for cloud tops are summarized in Fig. 6b. In every category the dimension increases by about 0.1 as the threshold is increased from base to top. Note that this threshold dependence of the perimeter dimension is opposite to the threshold dependence of the area enclosed by the perimeter (the exceedence set) as discussed for so-called "multifractals", (Hentschel and Procaccia 1983, 1984; Frisch and Parisi 1985). It is easy to see that the exceedence set dimension, which is related to its fractional area, must *decrease* as the threshold is raised. Since the perimeter is a subset of the exceedence set, its dimension is bounded by that of the exceedence set, so that it cannot increase indefinitely. The observed increase in the perimeter dimension may be related to an increased intensity of turbulence higher in the cloud. If so, one expects the vertical dependence to be different for different cloud types. For StCu the increase should be concentrated at cloud top, while in the ITCZ it is likely to occur through the full cloud thickness. Clearly more study is needed on this point.

b. Comparison of MSS and TM results

Analysis of Landsat-3 MSS and Landsat-4 TM data at Tel-Aviv University focused on fair weather cumulus clouds at four widely separated locations in the Pacific, east and west of the Florida peninsula, off West Africa, and in the Mediterranean. In addition, 11 Landsat-4 TM cases in the Florida area were analyzed (see Fig. 1). The average value of the perimeter fractal dimension, d_p, for all clouds below the break is 1.29 with a standard deviation of 0.04. The clouds larger than the cutoff have an average dimension of 1.54 with a standard deviation of 0.19. A value of 1.37, close to that of Lovejoy (1982) was found in only one case. The location of the break in slope averaged 0.5 km, and varied from 0.18 km to 1 km.

Figure 7 shows a comparison of the MSS results from Landsat-3 with the TM results from both Landsat-4 and Landsat-5 for fair weather cumulus cloud bases. Overall the agreement is excellent, especially considering the fact that different analysis techniques as well as different instruments were used. The Landsat-5 estimate of the dimension of the smaller clouds, 1.33, is a bit higher than the Landsat-3 and 4 estimates, given by 1.29 and 1.28, respectively. While the difference is barely within the error bars, it may nevertheless represent a real difference between the mainly Pacific Ocean cumulus used in the Landsat-5 estimate, and

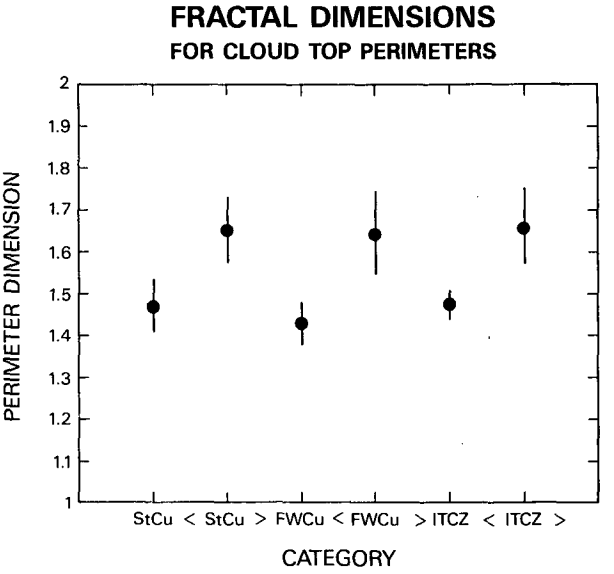

FIG. 6(b). As in Fig. 6(a), except for cloud top perimeters. Here we see violations of scaling for all three cloud types. Comparing with Fig. 6(a), we see that the perimeter fractal dimension increases with threshold. This is in contrast to the dimension of the enclosed area, which must decrease with threshold, and provides an upper bound to the perimeter dimension.

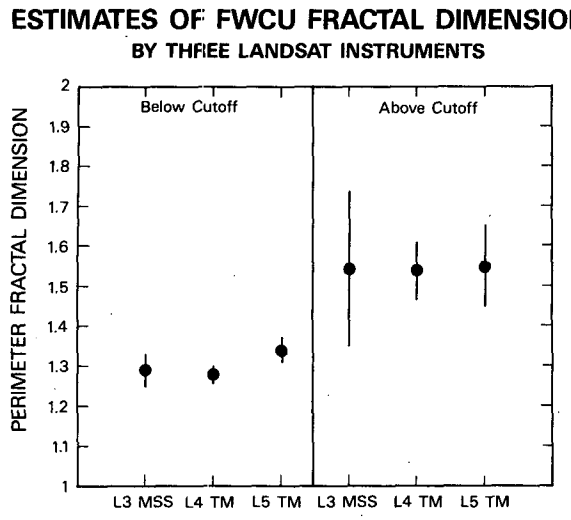

FIG. 7. Comparison of perimeter dimensions of smaller and larger fair weather cumulus clouds as estimated from data of the Landsat-3 MSS, Landsat-4 TM and Landsat-5 TM instruments. The values given in previous figures are from Landsat-5. given in previous figures are from Landsat-5.

the mainly Atlantic Ocean cumulus used in the Landsat-3 and 4 estimates.

The estimates shown in Fig. 7 of the fractal dimensions of the larger clouds have larger errors because there are fewer clouds in the larger size class. Despite this large variability of individual estimates, the mean values from all three instruments are in close agreement—1.54, 1,54 and 1.55 for Landsat-3, 4, and 5 respectively.

We compare the Tel-Aviv University (TAU) and Goddard Space Flight Center (GSFC) results for each region separately in Table 1. From Table 1a it may be seen that the fractal dimension of the perimeter of the smaller clouds determined from Landsat-3 MSS data over the Pacific Ocean is smaller than that of Landsat-5 TM. However, since the Pacific TM scenes are from a strip acquired on a single day, the 0.01 standard deviation shown may underestimate the actual variability.

Table 1b shows a comparison of Landsat-3 MSS and Landsat-4 TM results from various regions. None of the regional differences between the fair weather cumulus results are statistically significant. Thus, our results for the perimeter and area distributions may be taken as generally representative over the oceans. However, we reemphasize that we have not stratified our data seasonally, and since Landsat is sun-synchronous we have not been able to look for diurnal dependence.

c. *Physical interpretation*

Visual inspection of clouds above and below the break show that the smaller clouds usually have only one maximum of intensity, while the larger ones have a number of such maxima. This suggests cloud merging as a formation process for the larger clouds, which are more irregular in shape (higher fractal dimension) than the smaller ones, which may be produced directly by boundary layer convection. Perhaps the cutoff scale is determined by the thickness of the boundary layer, and the change in fractal dimension is related to a change from three-dimensional turbulence in the boundary layer to two-dimensional turbulence involving cloud mergers in the free atmosphere. There is clearly a need for more research on the factors determining the maximum size of convective cells, and more generally on the relation of different scaling regimes to different physical processes in the atmosphere.

TABLE 1a. Comparison of Landsat-3 and -5 results in the Pacific region.

	TAU Landsat-3 MSS	GSFC Landsat-5 TM
$d_p<$	1.27 ± 0.03	1.34 ± 0.01
$d_p>$	1.55 ± 0.06	1.47 ± 0.05

4. Summary and conclusions

We have estimated the probability distributions of cloud areas and perimeters of fair weather cumulus, stratocumulus and ITCZ clouds using thresholds for both cloud base and cloud top. To give an idea of the number of clouds on which these estimates are based, the values for the Landsat-5 TM fits are summarized in Table 2, which gives the number of cloud areas contributing to the fits of the number distribution (labeled "areas" in Table 2), and those contributing to fits of the perimeter-area plots ("perimeters" in Table 2). The total number of fair weather cumulus, stratocumulus and ITCZ clouds in the Landsat-5 TM database is 175 189 for the "base" threshold, and 169 938 for the "top" threshold. (One has fewer "tops" than "bases" for fair weather cumulus, since only the thickest and brightest ones exceed the "top" threshold; but a single stratocumulus "base" often has many "top" areas, which correspond to the many brightness variations one sees, despite the relatively constant cloud top height and temperature.) The total number of cloud base areas analyzed from all three satellite instruments is 405 598.

TABLE 1b. Comparison of Landsat-3 and -4 results in all regions.

Landsat number–region	$d_p<$	$d_p>$	Number of scenes
3—Pacific	1.27 ± 0.03	1.55 ± 0.06	3
3—Florida	1.30 ± 0.04	1.59 ± 0.17	10
3—West Africa	1.25 ± 0.02	1.56 ± 0.15	3
3—Israel	1.28	1.50	1
3—all	1.29 ± 0.04	1.54 ± 0.19	17
3—Florida	1.28 ± 0.02	1.55 ± 0.07	10

TABLE 2. Total number of clouds contributing to the parameters shown in Figs. 4 and 6 for the three cloud types, for both thresholds ("base" and "top"), and for both size categories ("<" and ">"). The total number of clouds analyzed may be obtained by adding $n<$ and $n>$ for StCu, FWCu, and ITCZ cloud bases, which gives 175 189. Note that StCu and ITCZ clouds have a greater number of contiguous cloud top areas than cloud base areas, unlike FWCu which have fewer. This is because most FWCu are single cells of varying thicknesses, while many of the StCu and ITCZ are multicell aggregates.

		Areas		Perimeters	
Type	Threshold	$n<$	$n>$	$p<$	$p>$
StCu	Base	22 997	593	5210	593
	Top	97 061	4334	24 217	4316
FWCu	Base	118 206	4945	47 433	4975
	Top	46 398	2928	19 885	2928
ITCZ	Base	27 063	1385	6206	1389
	Top	26 479	692	8056	692

Our results may be summarized as follows: The probability distributions of cloud areas and cloud perimeters are found to be approximately power-law, with powers denoted by $-2B$ and d_p, respectively. Stratocumulus clouds conform to a single power ($2B = 1.5$, $d_p = 1.4$) more closely than do fair weather cumulus. Fair weather cumulus exhibit a clear change in the fractal dimension, cloud bases less than about 0.5 km in diameter having a lower dimension ($2B = 0.6$, $d_p = 1.34$) than the larger clouds ($2B = 2.3$, $d_p = 1.55$). The fractal dimension also changes with the reflectivity threshold. As the threshold is raised from cloud base to cloud top, the perimeter fractal dimension increases, perhaps indicative of the increased turbulence at cloud top. In addition, scaling violations become evident at cloud top not only for fair weather cumulus but also for stratocumulus and ITCZ clouds.

The increase of the perimeter fractal dimension with threshold is especially interesting since the dimension of the enclosed areas, which provides an upper bound to the perimeter dimension, must *decrease*. A rather contrived example of such behavior is a field of grey circular disks of various sizes superimposed upon a black background, and each enclosing a white fractal snowflake with, say, half the area of the disk. A low threshold would show only the circles with $d_p = 1$, and a high threshold would show only the snowflakes with $d_p = 1.26$. This example is unrealistic because it has no scaling violations, but more important because it gives no physical basis for the increase of d_p. That must come from a three-dimensional model of cloud structure, and must be based upon the kind of turbulence and radiation properties appropriate for fair weather cumulus and stratocumulus clouds.

Why do fair weather cumulus larger than about 0.5 km show such strikingly different scaling behavior? Perhaps this break diameter represents the largest individual convective cells, and larger cumulus are aggregates of several such cells. An observation which seems to support this view is that in searching several cumulus scenes for cloud areas having a single peak in reflectivity, we did not find any larger than about 0.5 km, while there are many larger clouds with multiple brightness peaks. If this holds up in a more objective analysis of the full database, the question then becomes, What physically determines the maximum convective cell size?

This work is part of a growing body of observational evidence on inhomogeneous cloud structure. Derr and Gunter (1982) reported searching in vain for the sort of clouds assumed by cloud radiation modelers (whether plane-parallel or a lattice of simple shapes). Plots of liquid water along the aircraft track through Arctic stratus (the quintessential plane-parallel clouds) bounce between zero and high values in an erratic fashion.

One explanation of the ragged structure of clouds has emerged from the combined observational/theoretical study of Baker and Latham (1979). They find that the conventional assumption of homogeneous entrainment is incorrect; entrained dry air does not mix uniformly with cloudy air. Instead, it remains intact, as blobs of all sizes, which decay only slowly by invasion of cloudy air. Thus, in their model, a cloud is somewhat like Swiss cheese, although this analogy fails to convey the essence of cloud inhomogeneity since the size spectrum of holes in Swiss cheese is rather narrow.

Other implications of ragged cloud structure for climate modeling clearly also need further investigation. For example, the fractal stucture of clouds may explain the "optical depth paradox" (Wiscombe, et. al. 1984). On a zonal average, clouds behave as if they had optical depths less than ten or so, otherwise a cloud cover of roughly 50% cloud cover would have an albedo higher than 50% (the value needed to balance the radiation budget). On the other hand, extinction coefficients on the order of 30 km^{-1} are commonly calculated by cloud radiation modelers. If such values were correct, then the average cloud would be only about 300 m thick. This apparent contradiction may be due to our misconception of clouds as homogeneous objects.

Acknowledgments. The authors are grateful to Jon Robinson and Mark Nestler of Science Applications Research, Landover, Maryland, and Mrs. S. Rechavi, Mrs. Z. Rosen, and Mrs. S. Adler of Tel-Aviv University for significant scientific programming and analysis without which this study would not have been possible. We have also benefited from conversations with Drs. T. Bell, Harshvardan, R. Kahn, W. Ridgeway, and W. Wiscombe of the Goddard Laboratory for Atmospheres, and Professors Y. Mekler and B. Gelchinski of Tel-Aviv University. This study was funded in part by US AFOSR Grant 86-0174.

REFERENCES

Aida, M., 1977: Scattering of solar radiation as a function of cloud dimensions and orientation. *J. Quant. Spectrosc. Radiat. Transfer*, **17**, 303–310.

Baker, M. and J. Latham, 1979: The evolution of droplet spectra and the rate of production of embryonic raindrops in small cumulus clouds, *J. Atmos. Sci.*, **36**, 1612–1615.

Cahalan, R. F., D. A. Short and G. R. North, 1981: Cloud fluctuation statistics. *Mon. Wea. Rev.*, **110**, 26–43.

——, 1988: Landsat observations of fractal cloud structure, in Scaling, Fractals and Nonlinear Variability in Geophysics, Kluwer, in press.

Caughey, S. J., B. A. Crease and W. T. Roach, 1982: A field study of nocturnal stratocumulus II. turbulence structure and entrainment. *Quart. J. Roy. Meteor. Soc.*, **108**, 125–144.

Coakley, J. A., Jr., and F. P. Bretherton, 1982: Cloud cover from high-resolution scanner data: detecting and allowing for partially filled fields of view. *J. Geophys. Res.*, **87**, 4917–4932.

Davies, R., 1978: The effect of finite geometry on the three-dimensional transfer of solar irradiance in clouds. *J. Atmos. Sci.*, **35**, 1712–1725.

Derr, V. and R. Gunter, 1982: EPOCS 1980: Summary data report—Aircraft measurements of radiation, turbulent transport and profiles in the atmospheric and oceanic boundary layers of the tropical eastern pacific, NOAA Tech. Memo. ERL WPL-101.

Falconer, K. J., 1985: The Geometry of Fractal Sets, Cambridge University Press, 162 pp.

Farmer, J. D., E. Ott and J. A. Yorke, 1983: The dimension of chaotic attractors, *Physica*, **7D**, 153–180.

Frisch, U., and O. Parisi, 1985: On the singularity structure of fully developed turbulence. Turbulence and Predictability in Geophysical Fluid Dynamics and Climate Dynamics, Elsevier Science Publishers B. V., pp. 84–88.

Hahn, C. J., S. G. Warren, J. London, R. M. Chervin and R. Jenne, 1982: Atlas of simultaneous occurence of different cloud types over the ocean. NCAR Tech. Memo., NCAR/TN-201+STR. 212 pp.

Harshvardan, and J. A. Weinman, 1982: Infrared radiative transfer through a regular array of cuboidal clouds. *J. Atmos. Sci.*, **39**, 431–439.

Hentschel, H. G. E., and I. Procaccia, 1983: The infinite number of generalized dimensions of fractals and strange attractors. *Physica*, **8D**, 435–444.

——, and, ——, 1984: Relative diffusion in turbulent media, the fractal dimension of clouds. *Phys. Rev.*, **A29**, 1461–1476.

Hozumi, K., T. Harimaya and C. Magono, 1982: The size distribution of cumulus clouds as a function of cloud amount. *J. Meteor. Res. Japan*, **60**, 691–699.

Joseph, J. H., and R. F. Cahalan, 1988: Nearest neighbor spacing in fair weather cumulus as inferred from Landsat, *J. Clim. Appl. Meteor.*, submitted.

——, 1985: The role of cloud field morphology in weather and climate studies, *Isr. J. Earth Sci.*, **34**, 96–101.

Lovejoy, S., 1982: Area-perimeter relation for rain and cloud areas. *Science*, **216**, 185–187.

——, and B. B. Mandelbrot , 1985 : Fractal properties of rain and a fractal model. *Tellus*, **37A**, 209–232.

——, and D. Schertzer, 1985 : Generalized scale invariance in the atmosphere and fractal models of rain. *Water Resour. Res.*, **21**, 1233–1250.

Mandelbrot, B. B., 1983: The Fractal Geometry of Nature. W. H. Freeman, 460 pp.

——, 1986: Self-affine fractal sets. Parts I., II. and III., in Fractals in Physics, Elsevier Science Publishers B. V., pp. 3–28.

McKee, T. B., and J. T. Klehr, 1978: Effects of cloud shape on scattered solar radiation. *Mon. Wea. Rev.*, **106**, 399–404.

Plank, V. G. , 1969: The size distribution of cumulus clouds in representative Florida populations. *J. Appl. Meteor.*, **8**, 46–67.

Reynolds, P. D., T. B. McKee and K. L. Danielson , 1978: Effects of cloud size and cloud particles on satellite-observed reflected brightness. *J. Atmos. Sci.*, **35**, 160–164.

Schertzer, D., and S. Lovejoy, 1986: Generalized scale invariance and anisotropic inhomogeneous fractals in turbulence, Fractals in Physics, Elsevier Science Publishers B. V., pp. 457–460.

——, and ——, 1988: Multifractal simulations and analysis of clouds by multiplicative processes. *Atmos. Res.*, **21**, 337–361.

Rhys, Franz S., and A. Waldvogel , 1986: Fractal shape of hail clouds. *Phys. Rev. Lett.*, **56**, 784–787.

Wielicki, B. A., and R. M. Welch, 1986: Cumulus cloud properties derived using Landsat satellite data. *J. Climate Appl. Meteor.*, **25**, 261–276.

Wiscombe, W. J., R. M. Welch and W. D. Hall, 1984: The effects of very large drops on cloud absorption. I: Parcel models. *J. Atmos. Sci.*, **41**, 1336–1355.